INTERNATIONAL JOURNAL FOR NUMERICAL METHODS IN FLUIDS
Int. J. Numer. Meth. Fluids 2003; **41**:743–763 (DOI: 10.1002/fld.469)

Neural networks for BEM analysis of steady viscous flows

Nam Mai-Duy and Thanh Tran-Cong*,†

Faculty of Engineering and Surveying, University of Southern Queensland, Toowoomba, Qld 4350, Australia

SUMMARY

This paper presents a new neural network-boundary integral approach for analysis of steady viscous fluid flows. Indirect radial basis function networks (IRBFNs) which perform better than element-based methods for function interpolation, are introduced into the BEM scheme to represent the variations of velocity and traction along the boundary from the nodal values. In order to assess the effect of IRBFNs, the other features used in the present work remain the same as those used in the standard BEM. For example, Picard-type scheme is utilized in the iterative procedure to deal with the non-linear convective terms while the calculation of volume integrals and velocity gradients are based on the linear finite element-based method. The proposed IRBFN-BEM is verified on the driven cavity viscous flow problem and can achieve a moderate Reynolds number of 1400 using a relatively coarse uniform mesh. The results obtained such as the velocity profiles along the horizontal and vertical centrelines as well as the properties of the primary vortex are in very good agreement with the benchmark solution. Furthermore, the secondary vortices are also captured by the present method. Thus, it appears that an ability to represent the boundary solution accurately can significantly improve the overall solution accuracy of the BEM. Copyright © 2003 John Wiley & Sons, Ltd.

KEY WORDS: boundary element method; viscous flow problem; driven cavity flow; interpolation; indirect radial basis function network

1. INTRODUCTION

Boundary element method (BEM) has become a popular tool for analysis of engineering problems (e.g. Banerjee and Butterfield [1] and Brebbia *et al.* [2]). An advantage of the BEM is that the method allows the problem dimensionality to be reduced by one, resulting in relatively small system of equations in comparison with the ones associated with finite element method and finite difference method. In the standard BEM procedure, the boundary solution can be first obtained by solving a system of integral equations and the internal solution is then computed based on the boundary solution. For many linear problems such as potential flows governed by Laplace equation, linear elasticity (Navier equations) and viscous creeping flows (Stokes equations), the discretization of the governing equations needs to be performed on the boundary only. However, for non-linear or inhomogeneous problems, for example viscous

* Correspondence to: Thanh Tran-Cong, Faculty of Engineering and Surveying, University of Southern Queensland, Toowoomba, Qld. 4350, Australia.
† E-mail: trancong@usq.edu.au

Received 17 April 2002
Revised 16 October 2002

flows governed by Navier–Stokes equations or heat transfer problems governed by Poisson equation, discretization of the full domain is required due to the appearance of volume integrals. Nevertheless, the method is still attractive for solving certain classes of problems without large storage requirements. Recently, the particular solution technique (PS) (Zheng *et al.* [3]), dual reciprocity method (DRM) (Partridge *et al.* [4]) and multiple reciprocity method (MRM) (Nowak and Neves [5]) were developed successfully to reduce volume integrals to boundary integrals, which produce a true boundary integral formulation.

With regard to the numerical solution of viscous fluid flow problems, Kitagawa [6] and Power and Wrobel [7] gave excellent reviews of achievements by the BEM. The difficulties in solving the Navier–Stokes equations lie in the treatment of non-linear convective terms due to the lack of a fundamental solution corresponding to those equations. The first attempt to solve viscous incompressible flows at non-zero Reynolds numbers using boundary element formulation with the Stokeslet fundamental solutions was made by Bush and Tanner [8] where the convective terms, which generate volume integrals, were lumped together to form a forcing function (pseudo-body forces) and then handled via an iterative procedure using a successive substitution scheme. In that work, constant elements were used at the boundary while the velocity gradients and the volume integrals were treated by volume discretization using linear triangle elements with the nodal velocities taken from the previous iteration. Solutions were obtained at low Reynolds numbers (e.g. Re up to 30 for the Hamel flow problem). Tosaka and Onishi [9] enhanced the implementation of Bush and Tanner by utilizing a Newton–Raphson scheme for the solution of system of non-linear equations and also by integrating the volume integral by part in order to eliminate the need for the calculation of velocity gradients. The method was then applied to solve the driven cavity flow problem and the result was reported for the Reynolds number of 100 using a mesh of 82 linear boundary elements and 840 linear triangular interior cells. In Kitagawa *et al.*'s work [10], a penalty function formulation was used and the velocity gradients were calculated directly by differentiating the integral equations. In that work, the value of the penalty parameter was recommended to be of order $1.e4$ to $1.e6$ for general use. Numerical experiments showed that smaller values degrade the accuracy of the solution while larger values tend to spoil its convergence. The results of driven cavity flow were reported for the Reynolds number up to 400 using a non-uniform mesh of 160 linear boundary elements and 157 rectangular constant internal cells. Similarly, by using the PS technique/DRM instead of the cell integration approach, the BEM is still able to perform well for flows at low Reynolds numbers, but there is no indication that higher Reynolds number or accuracy are achieved. For example, the PS technique was applied to the case of the Hamel flow problem and also the plane jet problem (Zheng *et al.* [11]) and the maximum Reynolds numbers achieved were 40 and 14, respectively. The DRM was also tested in the case of steady viscous flow inside a closed circular cylindrical container, where the bottom and side walls are rotating with constant angular velocity while the top is fixed (Power and Partridge [12]) and numerical calculations were carried out for $Re = 1, 32$ and 100. Another approach based on the combination of an indirect BEM and DRM was applied to the study of 3D driven cavity viscous flow problem and the solution was given for $Re = 100$ (Power and Botte [13]). Recently, Florez *et al.* [14] stated that the traditional DRM approaches usually diverge for $Re > 200$ in complex flow configurations.

In the BEM literature, for the simulation of flows at higher Reynolds numbers, such as $Re = 1000$, to be successful, the BEM needs to be supplemented by some other features, e.g. higher order elements, adaptive integration, multiregion capability and velocity splitting

(Dargush and Banerjee [15]); domain decomposition and convective kernel (the use of convective kernel, instead of the usual Stokeslet one, was pioneered by Bush [16]) (Grigoriev and Fafurin [17] and Grigoriev and Dargush [18]); domain decomposition and DRM (Power and Mingo [19] and Florez *et al.* [14]); higher order domain cells, upwind and central finite difference approximations (Aydin and Fenner [20, 21]).

Recently, Mai-Duy and Tran-Cong [22] have shown that the indirect radial basis function networks (IRBFNs) perform better than element-based methods for function interpolation. In this paper, it is shown that the approximation of boundary solution by IRBFNs also significantly improves the performance of the BEM in terms of higher Reynolds number achievement and accuracy of the solution. By using the IRBFN interpolations to represent the variations of velocity and traction along the boundary from the nodal values while still keeping the use of Stokeslet fundamental solutions together with the standard treatments for the convective terms (e.g. a successive substitution scheme and linear cell approximations), the proposed IRBFN-BEM can achieve a Reynolds number of 1400 using a relatively coarse uniform mesh. Convergence is very slow at Reynolds number of 1400 which is here considered as a limit of the present approach, which does not give appropriate treatment to the convective term. Although the neural network approach can also be used in the treatment of the volume integral via the particular solution technique (Nguyen-Thien and Tran-Cong [23]), it is not employed here since the aim is to show that neural network approximation can be a better alternative to the traditional boundary element approximation and this comparison can only be done if all other parameters are kept the same as those reported in the literature. Furthermore, there is evidence to show that neither accuracy (Ingber *et al.* [24]) nor convergence (Power and Mingo [19]) is improved when volume integrals are approximated by similar techniques, such as dual reciprocity and particular solution. The results obtained by the present method such as the velocity profiles along the horizontal and vertical centrelines as well as the properties of the primary vortex are in very good agreement with the benchmark solution. Furthermore, the secondary vortices are also clearly captured. The paper is organized as follows. A brief review of indirect RBFN is given in Section 2 and in Section 3 the IRBFN is then introduced into the BEM scheme to approximate the boundary solution for analysis of steady viscous flow problems. In Section 4, the proposed method is verified through the simulation of driven cavity steady viscous flow. Section 5 gives some concluding remarks.

2. REVIEW OF IRBFNs

Radial basis function networks (RBFNs) for approximation and interpolation of function have received a great deal of attention over the last few decades (e.g. Haykin [25]). The RBF network allows a conversion of a function to be approximated from low dimension space (e.g. 1D–3D) to high dimensional space in which the function can now be expressed as a linear combination of radial basis functions

$$y(\boldsymbol{x}) \approx f(\boldsymbol{x}) = \sum_{i=1}^{m} w^{(i)} g^{(i)}(\boldsymbol{x}) \tag{1}$$

where m is the number of radial basis functions, $\{g^{(i)}\}_{i=1}^{m}$ is the set of chosen radial basis functions and $\{w^{(i)}\}_{i=1}^{m}$ is the set of weights to be found. It has been proved that RBFNs with one hidden layer are capable of universal approximation (Girosi and Poggio [26] and Park and

Sandberg [27]) and as a result, they take place in many applications in different disciplines. In the field of numerical solution of Partial Differential Equations (PDEs), some RBFNs were successfully used in the boundary element method to transform the volume integrals into equivalent boundary integrals (Zheng *et al.* [11] and Power and Partridge [12]). Furthermore, the networks were also developed successfully to solve PDEs in procedures which are regarded as truly mesh-free methods (e.g. References [28–31]). However, it should be noted that it is still very hard to achieve such an universal approximation RBFN in practice due to the difficulties associated with choosing the network parameters such as the number of radial basis functions, their positions and widths. In a previous work, Mai-Duy and Tran-Cong [22] proposed Indirect RBFNs (IRBFNs) which are based on the integration process, and their results showed that the IRBFNs perform better than the usual Direct RBFNs (DRBFNs) in terms of accuracy and convergence rate for both function and its derivatives. In this paper, the IRBFN is introduced into the BEM scheme to approximate the boundary solution for the analysis of 2D steady viscous fluid flow problems. In contrast to previous works [22, 30, 31] where the neural networks were used to approximate globally (meshless) the strong form of the governing equations (PDEs), the present work deals with the use of neural networks in the boundary element part of the mesh which discretises the inverse statement of the governing equations. In view of the fact that the BEM allows the reduction of the problem dimensionality by one, only the IRBFN for function and its derivatives (e.g. up to the second order) in 1D needs to be employed here and its formulation with multiquadric (MQ) is briefly recaptured as follows:

$$y''(s) \approx f''(s) = \sum_{i=1}^{m} w^{(i)} g^{(i)}(s) \tag{2}$$

$$y'(s) \approx f'(s) = \sum_{i=1}^{m} w^{(i)} H^{(i)}(s) + C_1 \tag{3}$$

$$y(s) \approx f(s) = \sum_{i=1}^{m} w^{(i)} \bar{H}^{(i)}(s) + C_1 s + C_2 \tag{4}$$

where s is the curvilinear co-ordinate (arclength), C_1 and C_2 are constants of integration and

$$g^{(i)}(s) = ((s - c^{(i)})^2 + a^{(i)2})^{1/2} \tag{5}$$

$$H^{(i)}(s) = \int g^{(i)}(s)\,\mathrm{d}s = \frac{(s - c^{(i)})((s - c^{(i)})^2 + a^{(i)2})^{1/2}}{2} + \frac{a^{(i)2}}{2} \ln((s - c^{(i)}) + ((s - c^{(i)})^2 + a^{(i)2})^{1/2}) \tag{6}$$

$$\bar{H}^{(i)}(s) = \int H^{(i)}(s)\,\mathrm{d}s = \frac{((s - c^{(i)})^2 + a^{(i)2})^{3/2}}{6} + \frac{a^{(i)2}}{2}(s - c^{(i)}) \ln((s - c^{(i)}) + ((s - c^{(i)})^2 + a^{(i)2})^{1/2}) - \frac{a^{(i)2}}{2}((s - c^{(i)})^2 + a^{(i)2})^{1/2} \tag{7}$$

in which $\{c^{(i)}\}_{i=1}^{m}$ is the set of centres and $\{a^{(i)}\}_{i=1}^{m}$ is the set of RBF widths. The RBF width is chosen based on the following simple relation:

$$a^{(i)} = \beta d^{(i)}$$

where β is a factor and $d^{(i)}$ is the minimum arclength between the ith centre and its neighbouring centres. Since C_1 and C_2 are to be found, it is convenient to let $w^{(m+1)} = C_1$, $w^{(m+2)} = C_2$, $\bar{H}^{(m+1)} = s$ and $\bar{H}^{(m+2)} = 1$ in (4) which becomes

$$y(s) \approx f(s) = \sum_{i=1}^{m+2} w^{(i)} \bar{H}^{(i)}(s) \tag{8}$$

$$\bar{H}^{(i)} = \text{RHS of (7)}, \quad i = 1, \ldots, m \tag{9}$$

$$\bar{H}^{(m+1)} = s \tag{10}$$

$$\bar{H}^{(m+2)} = 1 \tag{11}$$

The detailed implementation and accuracy of the IRBFN method were reported previously (Mai-Duy and Tran-Cong [22]). In the following section, the IRBFN is coupled with boundary integral equations for analysis of steady viscous fluid flows.

3. A NEW NEURAL NETWORK-BOUNDARY INTEGRAL APPROACH

3.1. Governing equations

The equations of motion and mass conservation for the steady flow of an incompressible viscous fluid can be written using Cartesian tensor notation as follows:

$$\mu u_{i,jj} - p_{,i} = \rho u_j u_{i,j} \tag{12}$$

$$u_{i,i} = 0 \tag{13}$$

where u_i is the velocity, ρ the fluid density, p the pressure and μ the viscosity. Equations (12)–(13) can be reformulated in terms of integral equations for a given spatial point $\mathbf{y}$ as follows:

$$c_{ij}(\mathbf{y}) u_j(\mathbf{y}) = \int_\Gamma U_{ij}(\mathbf{y}, \mathbf{x}) t_j(\mathbf{x}) \, \mathrm{d}\Gamma(\mathbf{x}) - \text{CPV} \int_\Gamma T_{ij}(\mathbf{y}, \mathbf{x}) u_j(\mathbf{x}) \, \mathrm{d}\Gamma(\mathbf{x}) + \rho \int_\Omega U_{ij}(\mathbf{y}, \mathbf{x}) b_j(\mathbf{x}) \, \mathrm{d}\Omega(\mathbf{x}) \tag{14}$$

$$U_{ij}(\mathbf{y}, \mathbf{x}) = \frac{1}{4\pi\mu} \left[\frac{r_i}{r} \frac{r_j}{r} - \delta_{ij} \ln(r) \right] \tag{15}$$

$$T_{ij}(\mathbf{y}, \mathbf{x}) = -\frac{1}{\pi r} \left[\frac{r_i}{r} \frac{r_j}{r} \frac{\partial r}{\partial n} \right] \tag{16}$$

where CPV is Cauchy principal value, U_{ij} and T_{ij} the Stokeslet fundamental solutions, u_j and t_j the velocity and the traction, respectively, $b_j = -u_k u_{j,k}$ the pseudo-body force containing

the convective term, c_{ij} the free term which is δ_{ij} if $\mathbf{y}$ is an internal point and $0.5\delta_{ij}$ if $\mathbf{y}$ is a point on the smooth boundary, $r_i = x_i - y_i$, $r = \|\mathbf{x} - \mathbf{y}\|$ and $\mathbf{n}$ the outwardly normal unit vector.

3.2. Approximation of the boundary solution by IRBFN

Integral equations allow the solving process to be confined to the boundary. After the process is done, the boundary solution obtained provides sources to compute the internal solution. It can be seen that the accuracy of the boundary solution greatly affects the accuracy of the overall solution. As mentioned earlier, neural networks are able to approximate arbitrarily well continuous functions. In this section, the IRBFNs are employed to represent the boundary solution. For simplicity of notation, the volume integral in (14) is ignored in the following discussion.

In the standard BEM, local interpolations are used to approximate the boundary solution via a subdivision of the boundary Γ into a number of small elements. On each element, the geometry and the variations of u_j and t_j are assumed to have a certain shape such as linear and quadratic ones. The CPV integrals can be indirectly computed by applying Equation (14) to represent rigid body displacements while the weakly singular ones can be evaluated using the well-known techniques such as logarithmic Gaussian quadrature and Telles' transformation technique (Telles [32]).

In the present method, global approximations using IRBFNs are employed. The boundary is also divided into a number of segments but with much larger size, provided that the associated boundaries are smooth and the prescribed boundary conditions are of the same type. On each segment, the variations of u_j and t_j and the curved geometry (if it exists) are approximated by neural networks. Due to the fact that none of basis functions employed in the network are null at the singular point (the point where the field point $\mathbf{x}$ and the source point $\mathbf{y}$ coincide), the method for evaluating the CPV integrals in the standard BEM cannot be applied directly here. To overcome this difficulty, the BIE formulation (14) needs to be rewritten in the form without CPV singularity as follows:

$$\int_\Gamma T_{ij}(\mathbf{y},\mathbf{x})(u_j(\mathbf{x}) - u_j(\mathbf{y}))\,\mathrm{d}\Gamma(\mathbf{x}) - \int_\Gamma U_{ij}(\mathbf{y},\mathbf{x})t_j(\mathbf{x})\,\mathrm{d}\Gamma(\mathbf{x}) = 0 \tag{17}$$

In the discretized form, Equation (17) becomes

$$\sum_{k=1}^{N_s} \int_{\Gamma_k} T_{ij}(\mathbf{y},\mathbf{x})(u_{j(k)}(\mathbf{x}) - u_{j(l)}(\mathbf{y}))\,\mathrm{d}\Gamma_k - \sum_{k=1}^{N_s} \int_{\Gamma_k} U_{ij}(\mathbf{y},\mathbf{x})t_{j(k)}(\mathbf{x})\,\mathrm{d}\Gamma_k = 0 \tag{18}$$

where N_s is the number of segments, subscript (k) denotes general segments and the subscript (l) indicates the segment containing the source point $\mathbf{y}$. The variations of velocity $u_{j(k)}$ and traction $t_{j(k)}$ on segment Γ_k are now represented by the IRBF networks in terms of the curvilinear co-ordinate s as (Equation (8))

$$u_{j(k)} = \sum_{i=1}^{mk+2} w_{u_{j(k)}}^{(i)} \bar{H}_{(k)}^{(i)}(s) \tag{19}$$

$$t_{j(k)} = \sum_{i=1}^{mk+2} w_{t_{j(k)}}^{(i)} \bar{H}_{(k)}^{(i)}(s) \tag{20}$$

where $s \in \Gamma_k$, mk is the number of training points on the segment k, $\{w_{u_{j(k)}}^{(i)}\}_{i=1}^{mk+2}$ and $\{w_{t_{j(k)}}^{(i)}\}_{i=1}^{mk+2}$ are the sets of weights of networks for the velocity $u_{j(k)}$ and traction $t_{j(k)}$ respectively. Similarly, the geometry can be interpolated from the nodal values by using IRBFNs as

$$x_{1(k)} = \sum_{i=1}^{mk+2} w_{x_{1(k)}}^{(i)} \bar{H}_{(k)}^{(i)}(s) \tag{21}$$

$$x_{2(k)} = \sum_{i=1}^{mk+2} w_{x_{2(k)}}^{(i)} \bar{H}_{(k)}^{(i)}(s) \tag{22}$$

Substitution of (19) and (20) into (18) yields

$$\sum_{k=1}^{N_s} \int_{\Gamma_k} T_{ij}(\mathbf{y},\mathbf{x}) \left(\sum_{i=1}^{mk+2} w_{u_{j(k)}}^{(i)} \bar{H}_{(k)}^{(i)}(s_{\mathbf{x}}) - \sum_{i=1}^{ml+2} w_{u_{j(l)}}^{(i)} \bar{H}_{(l)}^{(i)}(s_{\mathbf{y}}) \right) \mathrm{d}\Gamma_k$$
$$- \sum_{k=1}^{N_s} \int_{\Gamma_k} U_{ij}(\mathbf{y},\mathbf{x}) \left(\sum_{i=1}^{mk+2} w_{t_{j(k)}}^{(i)} \bar{H}_{(k)}^{(i)}(s_{\mathbf{x}}) \right) \mathrm{d}\Gamma_k = 0 \tag{23}$$

or,

$$\sum_{k=1}^{N_s} \left\{ \sum_{i=1}^{mk+2} w_{u_{j(k)}}^{(i)} \left(\int_{\Gamma_k} T_{ij}(\mathbf{y},\mathbf{x}) \bar{H}_{(k)}^{(i)}(s_{\mathbf{x}}) \, \mathrm{d}\Gamma_k \right) - \sum_{i=1}^{ml+2} w_{u_{j(l)}}^{(i)} \left(\int_{\Gamma_k} T_{ij}(\mathbf{y},\mathbf{x}) \bar{H}_{(l)}^{(i)}(s_{\mathbf{y}}) \, \mathrm{d}\Gamma_k \right) \right\}$$
$$- \sum_{k=1}^{N_s} \sum_{i=1}^{mk+2} w_{t_{j(k)}}^{(i)} \left(\int_{\Gamma_k} U_{ij}(\mathbf{y},\mathbf{x}) \bar{H}_{(k)}^{(i)}(s_{\mathbf{x}}) \, \mathrm{d}\Gamma_k \right) = 0 \tag{24}$$

where mk can vary from segment to segment. Equation (24) is formulated in terms of the IRBFN weights of networks for u_j and t_j rather than the nodal values of u_j and t_j as in the case of standard BEM. Clearly, the weakly singular integrals in (24) can be treated as in the case of standard BEM. The process of locating the source point $\mathbf{y}$ at all boundary training points results in an underdetermined system of non-linear equations with the unknown being the IRBFN weights. In the present work, an iterative procedure using Picard-type scheme is employed to render non-linear terms linear. A relaxation of the velocity field is applied at each iterative step and is discussed in Section 4.2 below. Thus, at each iteration, the system of linear equations obtained, which can have many solutions, needs to be solved in the general least squares sense. The preferred solution is the one whose values are smallest in the least squares sense (i.e. the norm of components is minimum). This can be achieved by using singular value decomposition technique (SVD). The procedural flow chart can be briefly summarized as follows:

1. Divide the boundary into a relatively small number of segments over each of which the boundary is smooth and the prescribed boundary conditions are of the same type;
2. Apply the IRBFNs for approximation of the prescribed physical boundary conditions in order to obtain IRBFN weights which are the boundary conditions in the weight space;
3. Initialize the velocity vector field and then compute the pseudo-body forces and the volume integrals. The latter are calculated using polar co-ordinates where the singularity

is weaken by the Jacobian before numerical integration by Gaussian quadrature is carried out (Ramachandran [33, p. 43]);
4. Form the system of equations and impose the boundary conditions obtained from the step 2;
5. Solve the system for IRBFN weights by SVD technique (under-determined system);
6. Compute the boundary solution by using the IRBFN interpolation;
7. Compute the velocity and its derivatives at internal points;
8. Check for convergence. Convergence measure (CM) at the kth iteration is defined as follows:

$$\mathrm{CM} = \sqrt{\frac{\sum_{i=1}^{n}[(u_1^k(\boldsymbol{x}^{(i)}) - u_1^{k-1}(\boldsymbol{x}^{(i)}))^2 + (u_2^k(\boldsymbol{x}^{(i)}) - u_2^{k-1}(\boldsymbol{x}^{(i)}))^2]}{\sum_{i=1}^{n}[(u_1^k(\boldsymbol{x}^{(i)}))^2 + (u_2^k(\boldsymbol{x}^{(i)}))^2]}}$$

where n is the number of boundary and internal points. The solution procedure is terminated when $\mathrm{CM} < \mathrm{tol}$, where tol is a set tolerance;
9. If not yet converged, relax the velocity field, update the pseudo-body forces, recompute the volume integral and then repeat from the step 5; or exit if it is deemed that the procedure will not converge;
10. If converged, output the results.

Note that the system matrix obtained at the step 4 depends only on the geometry of the problem and hence the SVD needs to be done only once at the first iteration while the RHS vector containing the volume integrals is updated during the iteration process.

4. NUMERICAL RESULTS

4.1. General results

The benchmark problem of steady viscous flow in an unitary square cavity (Roache [34]) is simulated in this section to verify the present method. The top wall moves with a uniform velocity of 1 in its own plane while the other walls are fixed (Figure 1). Here the Reynolds number is defined as $Re = \rho UH/\mu$, where U is the characteristic velocity, H the characteristic length, ρ the density and μ the viscosity. This problem is geometrically simple and used for decades as a test problem to verify and validate numerical methods in computational science and engineering. Ghia *et al.* [35] produce a benchmark solution that is often cited for comparison purposes.

There are many works in literature using BEM to simulate the driven cavity steady viscous flow. For the simulation of flows at moderate and high Reynolds numbers, recent trends are to incorporate BEM with domain decomposition techniques or to use high order volume elements for the evaluation of the volume integrals.

In the present work, the idea is to use the IRBFN interpolations to represent the boundary solution. To check the effect of this proposal, the other features used here remain the same as those used in Bush and Tanner's work [8], for the reasons explained earlier in the introduction: e.g. Picard-type iterations are applied and linear cell-based approximations are employed to treat the volume integral and the velocity gradient. Note that all the following numerical solutions for each Reynolds number are obtained starting from the condition of fluid at rest

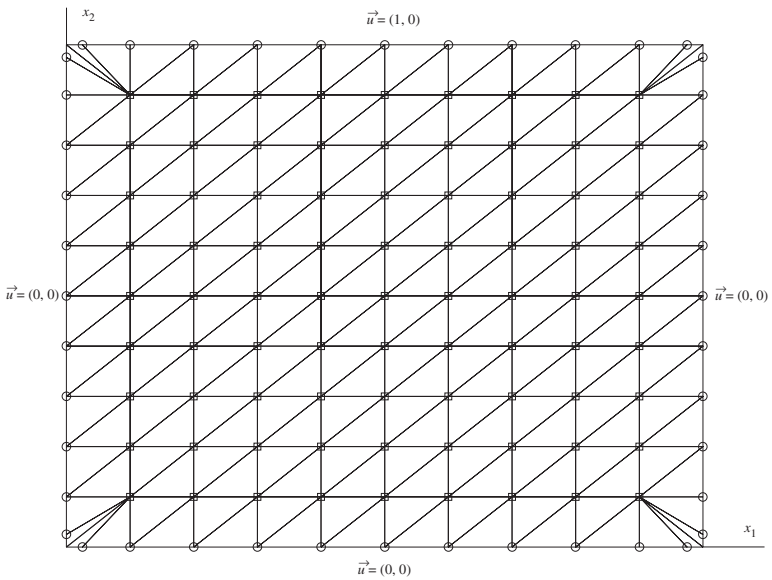

Figure 1. Driven cavity flow problem: geometry definition, boundary condition and discretization. Legends ○: boundary point and □: internal point. The boundary is simply represented by the set of points (i.e. there are no boundary elements involved in variable interpolation). The volume cells are the same as in other comparative works.

Table I. Driven cavity viscous flow: a number of meshes are used for the study of convergence.

Mesh	Boundary points	Internal points	Triangle elements
11×11	11×4	9×9	208
17×17	17×4	15×15	520
21×21	21×4	19×19	808
33×33	33×4	31×31	2056

and the tolerance for convergence criterion is set at $\text{tol} = 5e - 3$. The factor β is chosen to be unity, except where otherwise stated. The boundary of domain is divided into 4 segments corresponding to the four edges of the cavity and on each segment, the set of boundary points becomes the set of centres and also the set of collocation points of the network. In order to be able to present the correct description of multivalued traction at the corner, the extreme centres on each segment are shifted into the segment by a 1/4 of the distance between two adjacent centres (Figure 1). A number of uniform data meshes, namely 11×11 (i.e. 11×4 boundary points and 9×9 internal points), 17×17, 21×21 and 33×33 (Table I), are utilized for the study of mesh convergence. For Reynolds number $Re = 100$, four meshes are employed. The velocity profiles along the vertical and horizontal centrelines obtained by the present IRBFN-BEM together with the benchmark solution by Ghia *et al.* [35] are displayed in Figure 2(a) and 2(b) showing that close agreements are achieved. Figure 2(c) shows the

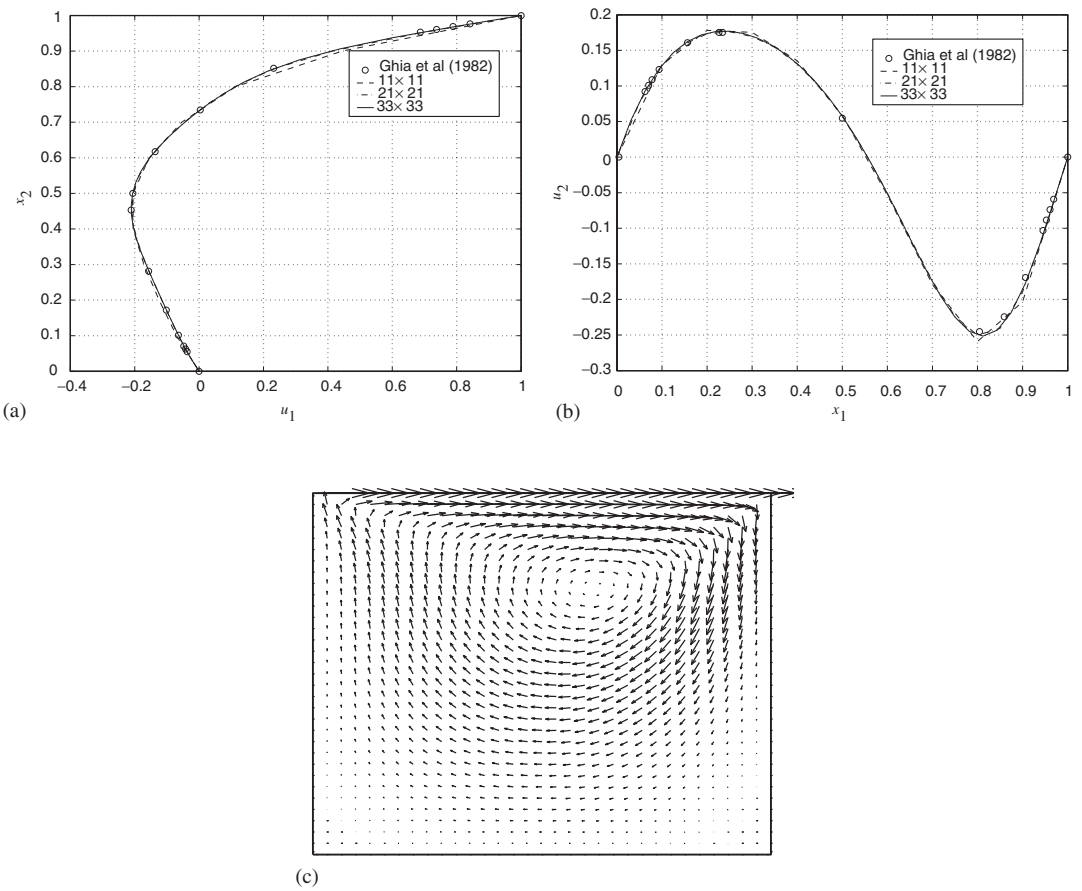

Figure 2. Driven cavity flow, $Re = 100$: mesh convergence by the present IRBFN-BEM. Legend ○ denotes the result obtained by Ghia *et al.* [35]. The velocity vector field obtained with a mesh 33×33 is also displayed. (a) u_1 on the vertical centreline; (b) u_2 on the horizontal centreline; (c) velocity vector field.

velocity vector field obtained using the finest mesh. For the purpose of checking the effect of β on the solution, another test is also done with the mesh of 11×11. The present method converges for all values of β in the range of 1–9 with an increment of 2, and all solutions agree well with the benchmark solution, which shows that the BEM solution is relatively independent of the value of RBF width. For moderate Reynolds numbers of 400 and 1000, the last three meshes are used to simulate the flows. As shown in Figures 3 and 4, there are good agreements between the present results and the benchmark solution even in the case of very coarse mesh of 17×17. The achieved solution with the coarse mesh of 17×17 seems to indicate that the IRBFN interpolation yields superior accuracy in solving PDEs.

Other important results are the properties of the primary vortex and the existence of secondary vortices at the bottom corners. However, only few works in the BEM literature mention

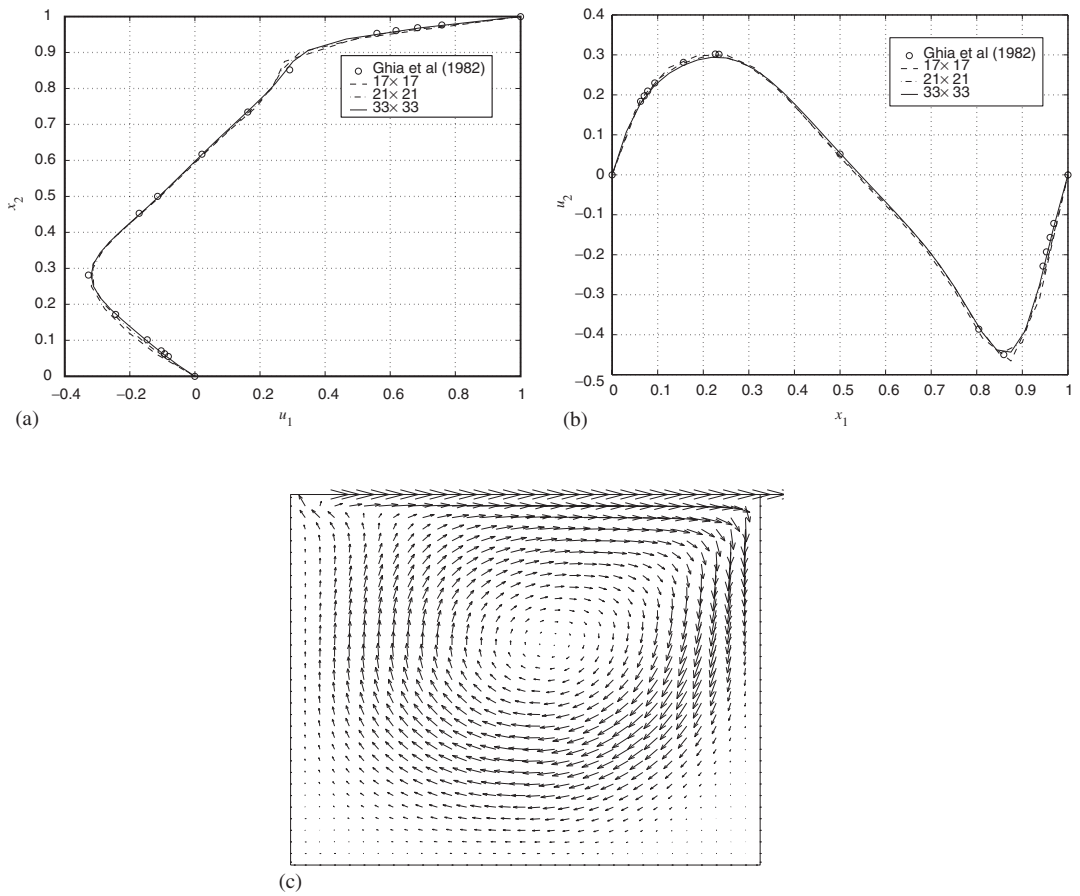

Figure 3. Driven cavity flow, $Re = 400$: mesh convergence by the present IRBFN-BEM. Legend ○ denotes the result obtained by Ghia *et al.* [35]. The velocity vector field obtained with a mesh 33×33 is also displayed. (a) u_1 on the vertical centreline; (b) u_2 on the horizontal centreline; (c) velocity vector field.

those results. In the present work, the secondary vortices are captured and shown in Figures 5 and 6. Both secondary vortices at the bottom corners can be seen clearly using a mesh of 33×33 while in the work by Aydin and Fenner [20], where a mesh of 41×41 was used, the centre of the vortex at the left hand corner is not well defined and appears to be close to the bottom boundary. Several properties of the primary vortex such as the location and the minimum value of stream-function are given in Table II, showing that the present method yields high accuracy in the primary vortex region. From Table II and Figures 2(c)–4(c), it can be seen that the location of the vortex centre appears near the top right corner at $Re = 100$ and then moves towards the geometric center of the cavity as the Reynolds number increases. Figure 7 demonstrate the thinning of the boundary layers as the Reynolds number increases

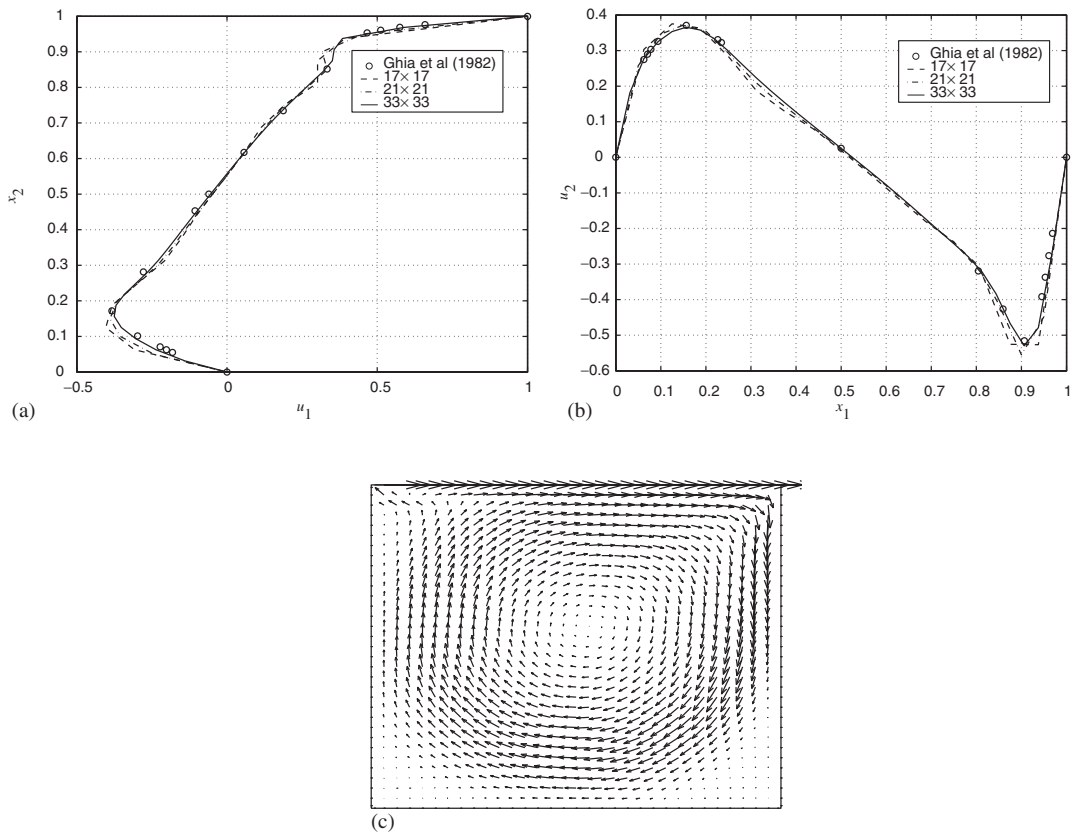

Figure 4. Driven cavity flow, $Re = 1000$: mesh convergence by the present IRBFN-BEM. Legend ○ denotes the result obtained by Ghia *et al.* [35]. The velocity vector field obtained with a mesh 33×33 is also displayed. (a) u_1 on the vertical centreline; (b) u_2 on the horizontal centreline; (c) velocity vector field.

which is consistent with the results by Ghia *et al.* [35]. Since a result for the Reynolds number of 1400 is not available, the result for the Reynolds number of 1000 is included in the figure to demonstrate both the thinning of the boundary layers and the physical feasibility of the solution.

The overall sense of solution accuracy can also be measured by computing the bulk continuity of the flow. For the driven cavity flow this is commonly achieved by computing the flow rate across the vertical plane (Q_1) and the horizontal plane (Q_2) passing through the geometric centre of the cavity. A more accurate solution would necessarily yield both flow rates closer to the exact value of zero. The flow rates Q_1, Q_2 for the three most refined meshes and the three Reynolds numbers (100, 400, 1000) are shown in Tables III and IV. The results show that the flow rates consistently tend to zero as the mesh density increases for all Reynolds numbers.

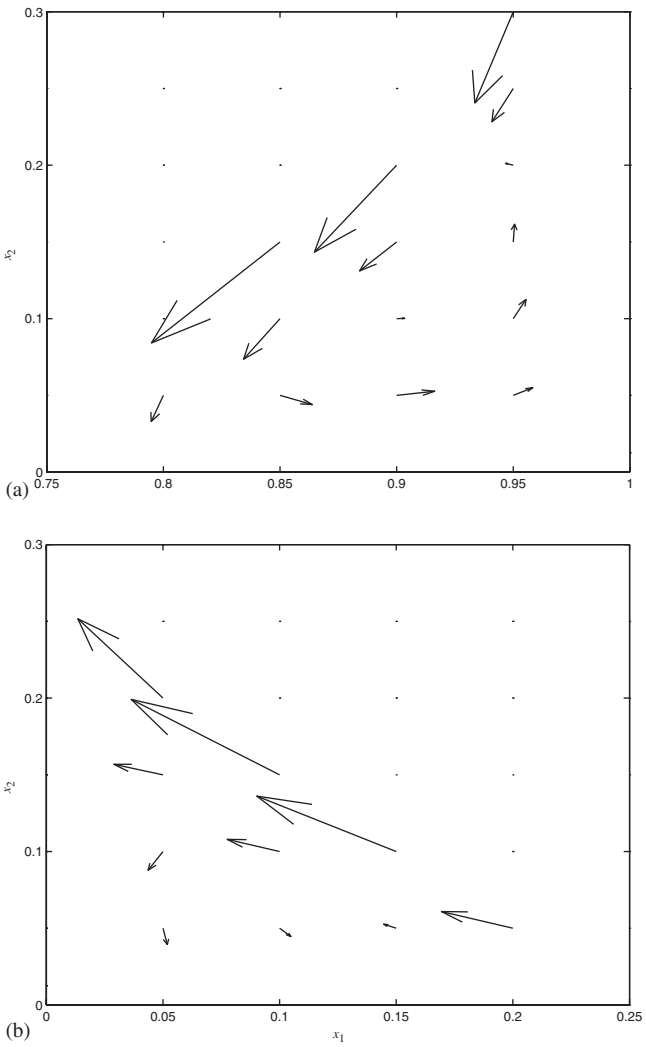

Figure 5. Driven cavity flow, $Re = 1000$: the plot of secondary vortices captured using a mesh of 21×21. (a) Secondary vortex at the right corner; (b) secondary vortex at the left corner.

4.2. *Relaxation in the iterative procedure*

In the case of higher Reynolds number ($Re \geqslant 400$), it is necessary to relax the iterative process by applying a relaxation factor to the velocity field according to

$$u_i = \alpha u_i^k + (1 - \alpha) u_i^{k-1}$$
$$u_{i,j} = \alpha u_{i,j}^k + (1 - \alpha) u_{i,j}^{k-1}$$

where α denotes the relaxation factor and the superscript k indicates the current iteration.

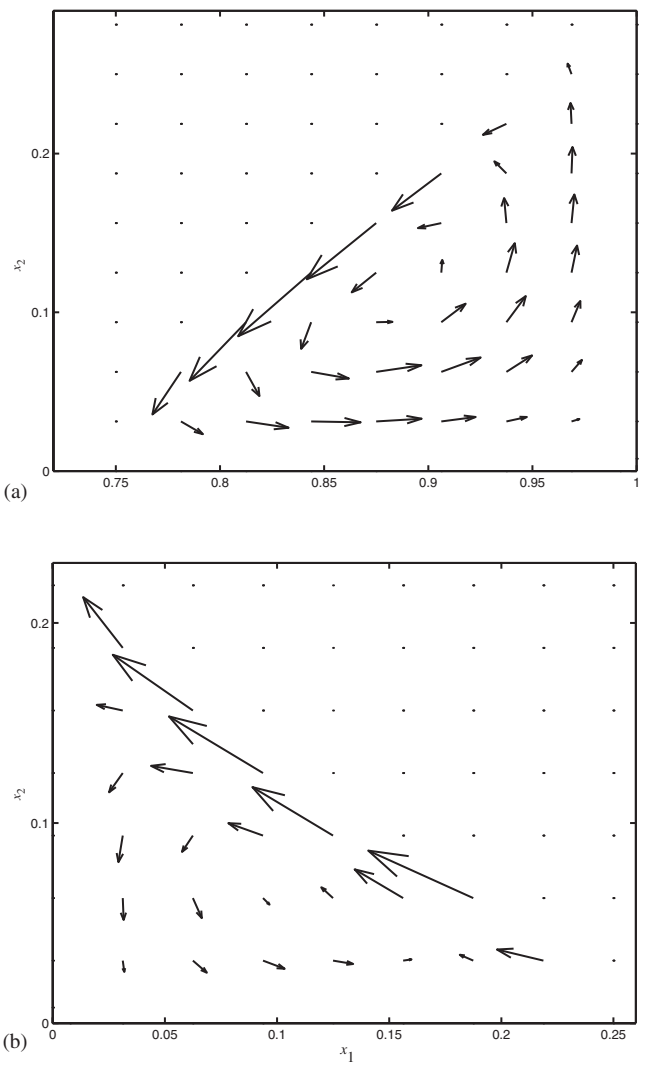

Figure 6. Driven cavity flow, $Re = 1000$: the plot of secondary vortices captured using a mesh of 33×33. (a) Secondary vortex at the right corner; (b) secondary vortex at the left corner.

In general, it is observed that when the process is slightly relaxed (high relaxation factor α), or not at all relaxed ($\alpha = 1$), the process is usually either non-convergent or fast convergent. There are also some oscillations in an otherwise convergent process. It is found that the iterative process behaves consistently where the convergence characteristics is slower, but smoother, for smaller relaxation factors (Figure 8(a) and 8(b)). In Figure 8(a), the corresponding results for the standard BEM are also presented. For the same relaxation factor, the standard BEM either does not perform as well in the case of relaxation factor of 0.05, or

Table II. Driven cavity viscous flow: comparison of the properties of the primary vortex obtained by the present IRBFN-BEM and the benchmark solution (Ghia *et al.* [35]).

	$Re=100$		$Re=400$		$Re=1000$	
	$\psi_{\min}$	Position	$\psi_{\min}$	Position	$\psi_{\min}$	Position
Bench. (129×129)	-0.103	$(0.617, 0.734)$	-0.114	$(0.555, 0.606)$	-0.118	$(0.531, 0.563)$
Present (17×17)	-0.103	$(0.612, 0.736)$	-0.116	$(0.551, 0.598)$	-0.122	$(0.539, 0.558)$
Present (21×21)	-0.103	$(0.614, 0.737)$	-0.113	$(0.553, 0.601)$	-0.119	$(0.536, 0.558)$
Present (33×33)	-0.103	$(0.616, 0.737)$	-0.112	$(0.556, 0.603)$	-0.117	$(0.533, 0.561)$

$\psi_{\min}$ denotes the minimum value of stream-function.

Table III. Driven cavity viscous flow: volumetric flow rate across the vertical plane defined by $Q_1=1/Q_c\int u_1(x_1=0.5,x_2)\,dx_2$, where Q_c is a characteristic flow rate and chosen to be $UH/2$ as in Aydin and Fenner [20] (i.e. the rate of the Couette flow when ignoring two vertical walls).

Mesh	$Re=100$	$Re=400$	$Re=1000$
17×17	0.0030	-0.0049	-0.0179
21×21	0.0027	-0.0018	-0.0100
33×33	0.0019	0.0006	-0.0023

Note: Simpson's rule is applied to compute the integral. For each of the Reynolds numbers, the value of the flow rate Q_1 consistently approaches zero as the mesh density is increased, which shows that mesh convergence is achieved for all of the cases studied here.

Table IV. Driven cavity viscous flow: volumetric flow rate across the horizontal plane defined by $Q_2=1/Q_c\int u_2(x_1,x_2=0.5)\,dx_1$, where Q_c is a characteristic flow rate and chosen to be $UH/2$ as in Aydin and Fenner [20] (i.e. the rate of the Couette flow when ignoring two vertical walls).

Mesh	$Re=100$	$Re=400$	$Re=1000$
17×17	-0.0021	-0.0133	-0.0302
21×21	-0.0014	-0.0079	-0.0177
33×33	-0.0006	-0.0028	-0.0062

Note: The integral is calculated using Simpson's rule. For each of the Reynolds numbers, the value of the flow rate Q_2 consistently approaches zero as the mesh density is increased, which shows that mesh convergence is achieved for all of the cases studied here.

behaves badly in the case of relaxation factor of 0.07, which is contrary to expectation that a higher relaxation factor should make convergence faster. Finally, for a given relaxation factor, Figure 9 illustrates an important convergence characteristics of the present method where the convergence rate improves with increasing mesh density.

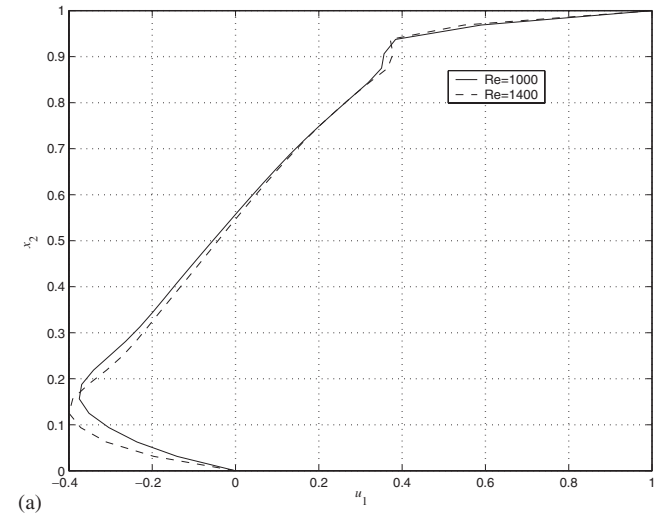

(a)

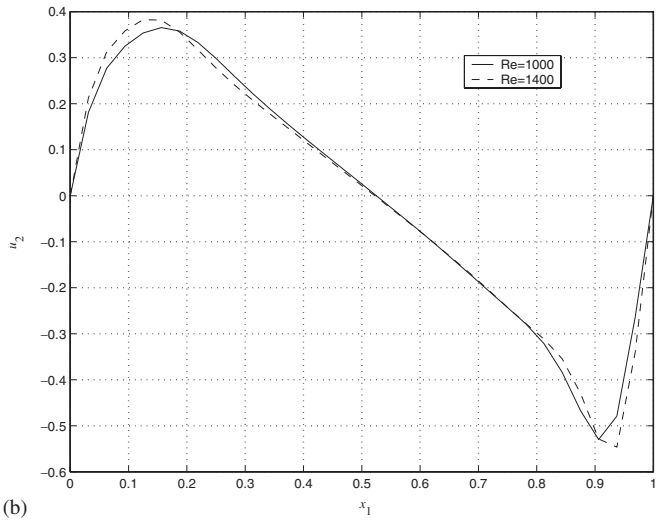

(b)

Figure 7. Driven cavity flow, $Re = 1400$, mesh density of 33×33: Plots of velocity profile along the vertical and horizontal centrelines. The results for $Re = 1000$ is also displayed. It can be seen that the velocity profiles and also the velocity vector field (not displayed here for simplicity) are similar between the two Reynolds numbers, however the boundary layers of the higher Reynolds number appear to be thinner. (a) u_1 on the vertical centreline; (b) u_2 on the horizontal centreline.

4.3. Comparison with standard BEM results

Apart from the above comparison of the present results with the benchmark results of Ghia *et al.* [35], comparison with the standard linear BEM results is also made in this section to demonstrate the improvement achieved by the present method. It is reiterated here that the

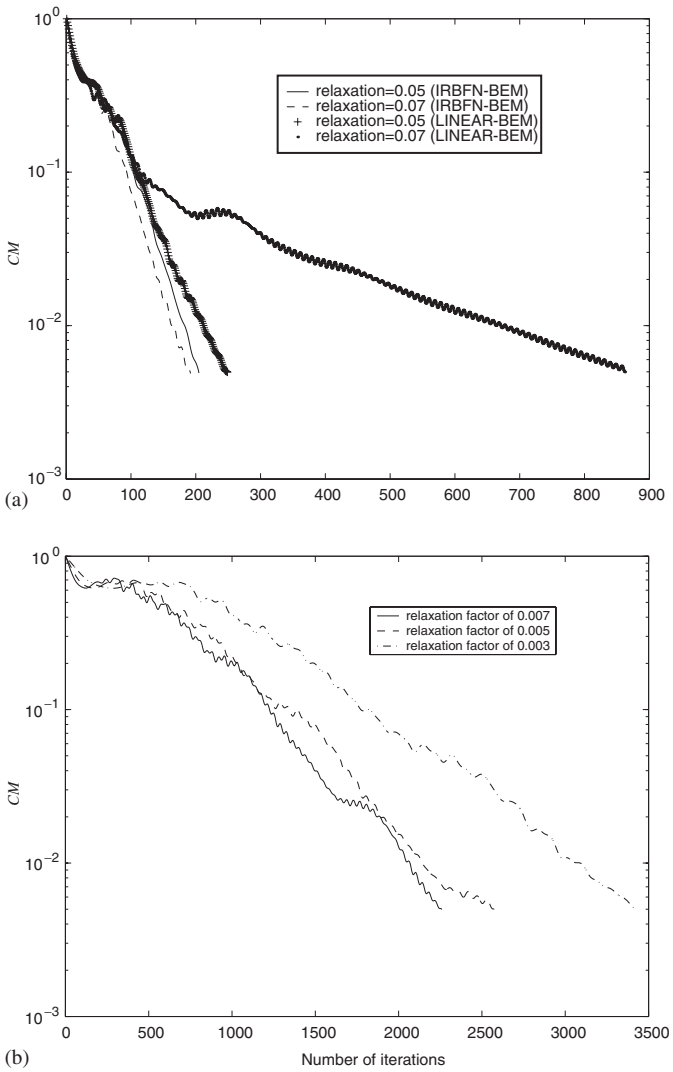

Figure 8. Driven cavity flow, mesh density of 17×17: Effect of the relaxation factor on the convergence rate for (a) $Re = 400$ and (b) $Re = 1000$. In Figure 8(a), the results obtained by the standard Linear-BEM are also included for the purpose of comparison.

general computational algorithm for the two methods are the same and the only distinguishing feature between the two methods is that neural network approximation instead of conventional Lagrange polynomial approximation is used in boundary elements. The comparison is based on three aspects, namely solution accuracy, Reynolds number limit and computational time. Figure 10 demonstrates the improvement in solution accuracy achieved by the present method over the standard BEM results. The standard BEM fails to converge at Reynolds numbers greater than 400 irrespective of the relaxation treatment whereas the Reynolds number of

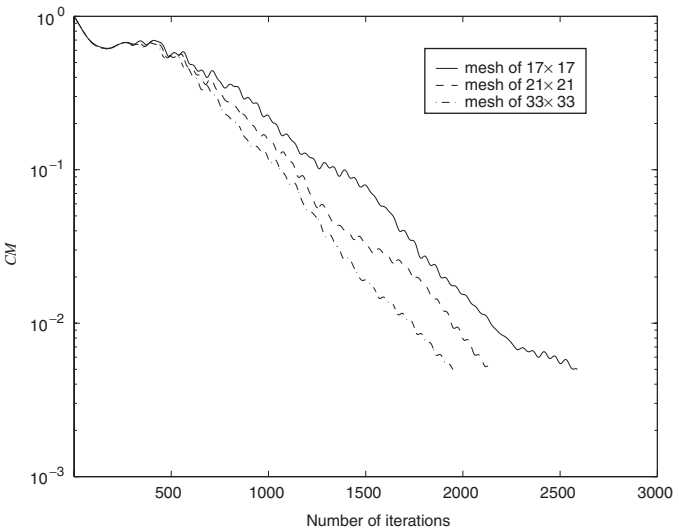

Figure 9. Driven cavity flow problem, $Re = 1000$, relaxation factor of 0.005: Effect of mesh density on the convergence rate. A higher mesh density consistently yields a faster convergence rate.

Table V. Driven cavity viscous flow, $Re = 100$, relaxation factor of 0.7: total CPU time used to obtain a converged solution by Linear-BEM and IRBFN-BEM.

Mesh	Linear-BEM		IRBFN-BEM	
	Matrix size	CPU time (s)	Matrix size	CPU time (s)
11×11	88×88	176	88×104	109
17×17	136×136	762	136×152	584
21×21	168×168	1703	168×184	1352

Note: The code is written in the MATLAB language (version R11.1 by The MathWorks, Inc.), which was run on a 1000 MHz Pentium PC. Note that MATLAB language is interpretative.

1400 is achieved by the present method. In terms of computational time, Table V shows that the present method achieves a significant improvement in efficiency despite the fact that the system matrix is slightly bigger for the same mesh density.

5. CONCLUDING REMARKS

This paper presents a new approach for analysis of steady viscous flow problems in which indirect RBFNs are introduced into the BEM scheme to approximate the boundary solution. Global approximations using neural networks are employed along the boundary instead of local approximations based on Lagrange polynomials. Numerical results obtained show that the BEM solution is significantly improved in terms of Reynolds number achievement and

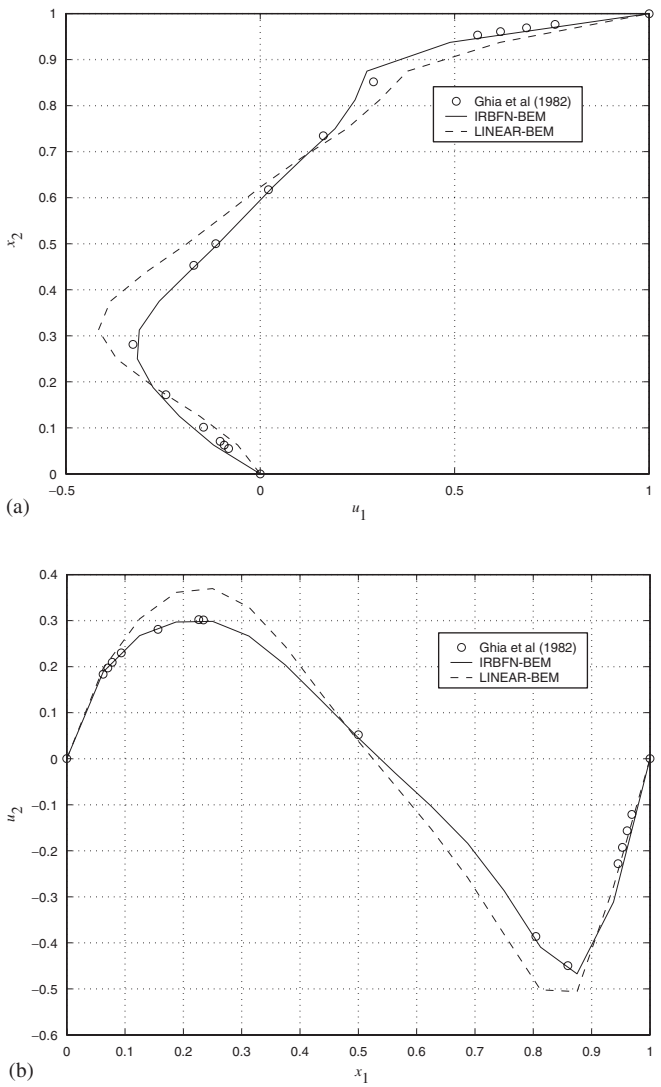

Figure 10. Driven cavity flow, $Re = 400$, mesh density of 17×17: Comparison of velocity profiles along the horizontal and vertical centrelines obtained by the present IRBFN-BEM and the standard linear-BEM. (a) v_1 on the vertical centreline; (b) v_2 on the vertical centre line.

accuracy of the solution. Thus, this new approach is an alternative that can enhance the performance of the BEM for analysis of steady viscous flow. The improvement can be attributed to the ability to represent the boundary solution accurately by the present IRBFNs. The present method described in this paper is general and can be used to solve other non-linear problems such as non-Newtonian flow problems, provided the non-linearity in the problem can be lumped into the body-force term.

ACKNOWLEDGEMENTS

The authors would like to thank the referees for their helpful comments.

REFERENCES

1. Banerjee PK, Butterfield R. *Boundary Element Methods in Engineering Science*. McGraw-Hill: London, 1981.
2. Brebbia CA, Telles JCF, Wrobel LC. *Boundary Element Techniques*: *Theory and Applications in Engineering*. Springer-Verlag: Berlin, 1984.
3. Zheng R, Coleman CJ, Phan-Thien N. A boundary element approach for non-homogeneous potential problems. *Computational Mechanics* 1991; **7**:279–288.
4. Partridge PW, Brebbia CA, Wrobel LC. *The Dual Reciprocity Boundary Element Method*. Computational Mechanics Publications: Southampton, 1992.
5. Nowak AJ, Neves AC. *The Multiple Reciprocity Boundary Element Method*. Computational Mechanics Publications: Southampton, 1994.
6. Kitagawa K. *Lecture Notes in Engineering. vol. 55*: *Boundary Element Analysis of Viscous Flow*. Springer-Verlag: Berlin, 1990.
7. Power H, Wrobel LC. *Boundary Integral Methods in Fluid Mechanics*. Computational Mechanics Publications: Southampton, 1995.
8. Bush MB, Tanner RI. Numerical solution of viscous flows using Integral Equation Methods. *International Journal for Numerical Methods in Fluids* 1983; **3**:71–92.
9. Tosaka N, Onishi K. Boundary integral equations formulations for steady Navier–Stokes equations using the Stokes fundamental solution. *Engineering Analysis* 1985; **2**(3):128–132.
10. Kitagawa K, Brebbia CA, Wrobel LC, Tanaka M. Boundary element analysis of viscous flow by penalty function formulation. *Engineering Analysis* 1986; **3**(4):194–200.
11. Zheng R, Phan-Thien N, Coleman CJ. A boundary element approach for non-linear boundary-value problems. *Computational Mechanics* 1991; **8**:71–86.
12. Power H, Partridge PW. The use of Stokes's fundamental solution for the boundary only formulation of the three-dimensional Navier–Stokes equations for moderate Reynolds numbers. *International Journal for Numerical Methods in Engineering* 1994; **37**:1825–1840.
13. Power H, Botte V. An indirect boundary element method for low Reynolds number Navier–Stokes equations in a three-dimensional cavity. *International Journal for Numerical Methods in Engineering* 1998; **41**:1485–1505.
14. Florez W, Power H, Chejne F. Multi-domain dual reciprocity BEM approach for the Navier–Stokes system of equations. *Communications in Numerical Methods in Engineerings* 2000; **16**:671–681.
15. Dargush GF, Benerjee PK. Boundary element method for steady incompressible thermoviscous flow. *International Journal for Numerical Methods in Engineering* 1991; **31**:1605–1626.
16. Bush MB. Modelling two-dimensional flow past arbitrary cylindrical bodies using boundary element formulations. *Applied Mathematical Modelling* 1983; **7**:386–394.
17. Grigoriev MM, Fafurin AV. A boundary element method for steady viscous fluid flow using penalty function formulation. *International Journal for Numerical Methods in Fluids* 1997; **25**:907–929.
18. Grigoriev MM, Dargush GF. A poly-region boundary element method for incompressible viscous fluid flows. *International Journal for Numerical Methods in Engineering* 1999; **46**:1127–1158.
19. Power H, Mingo R. The DRM subdomain decomposition approach to solve the two-dimensional Navier–Stokes system of equations. *Engineering Analysis with Boundary Elements* 2000; **24**(1):107–119.
20. Aydin M, Fenner RT. Boundary element analysis of driven cavity flow for low and moderate Reynolds numbers. *International Journal for Numerical Methods in Fluids* 2001; **37**:45–64.
21. Aydin M, Fenner RT. Boundary element analysis of viscous channel flow. *Numerical Heat Transfer*, *Part A* 2000; **38**:755–793.
22. Mai-Duy N, Tran-Cong T. Mesh-free radial basis function network methods with domain decomposition for approximation of functions and numerical solution of Poisson's equations. *Engineering Analysis with Boundary Elements* 2002; **26**:133–156.
23. Nguyen-Thien T, Tran-Cong T. BEM-neural network approach for polymeric liquids flow analysis. *Engineering Analysis with Boundary Elements* 2000; **24**(1):95–106.
24. Ingber MS, Mammoli AA, Brown MJ. A comparison of domain integral evaluation techniques for boundary element methods. *International Journal for Numerical Methods in Engineering* 2001; **52**:417–432.
25. Haykin S. *Neural Networks: A Comprehensive Foundation*. Prentice-Hall: Englewood Cliffs, NJ, 1999.
26. Girosi F, Poggio T. Networks and the best approximation property. *Biological Cybernetics* 1990; **63**:169–176.
27. Park J, Sandberg IW. Universal approximation using radial basis function networks. *Neural Computation* 1991; **3**:246–257.

28. Kansa EJ. Multiquadrics—A scattered data approximation scheme with applications to computational fluid-dynamics-II. Solutions to parabolic, hyperbolic and elliptic partial differential equations. *Computers and Mathematics with Applications* 1990; **19**(8/9):147–161.
29. Zerroukat M, Power H, Chen CS. A numerical method for heat transfer problems using collocation and radial basis functions. *International Journal for Numerical Methods in Engineering* 1998; **42**:1263–1278.
30. Mai-Duy N, Tran-Cong T. Numerical solution of differential equations using multiquadric radial basis function networks. *Neural Networks* 2001; **14**(2):185–199.
31. Mai-Duy N, Tran-Cong T. Numerical solution of Navier–Stokes equations using multiquadric radial basis function networks. *International Journal for Numerical Methods in Fluids* 2001; **37**:65–86.
32. Telles JCF. A self-adaptive co-ordinate transformation for efficient numerical evaluation of general boundary element integrals. *International Journal for Numerical Methods in Engineering* 1987; **24**:959–973.
33. Ramachandran PA. *Boundary Element Methods in Transport Phenomena*. Computational Mechanics Publications: Southampton, 1994.
34. Roache PJ. *Verification and Validation in Computational Science and Engineering*. Hermosa Publishers: Albuquerque, 1998.
35. Ghia U, Ghia KN, Shin CT. High-Re solutions for incompressible flow using the Navier–Stokes equations and a multigrid method. *Journal of Computational Physics* 1982; **48**:387–411.

